



Original Contribution

Design of a Phantom Mimicking Rectal Lymph Nodes for Magnetomotive Ultrasound

Arefeh Mousavi^a, Jules Reniaud^b, Magnus Santesson^a, Linda Persson^a, Tomas Jansson^{b,c,*}

^a NanoEcho AB, Lund, Sweden

^b Department of Clinical Sciences Lund/Biomedical Engineering, Lund University, Lund, Sweden

^c Digitalisering IT/MT, Skåne Regional Council, Lund, Sweden

ARTICLE INFO

Keywords:

Ultrasound phantom
Styrene-butylene/ethylene-styrene
Polyvinyl alcohol
Rectal cancer
Elasticity
Magnetic nanoparticles
Contrast agents

ABSTRACT

Objective: Durable and stable phantoms for verifying and validating the new magnetomotive ultrasound technique are lacking. Here we propose a phantom design to address this need.

Methods: A mixture of styrene-butylene/ethylene-styrene (SEBS) in mineral oil and glass beads as a scattering material acted as a bulk material, in which a polyvinyl alcohol (PVA) inclusion containing magnetic nanoparticles in water solution and graphite was embedded. The design mimics nanoparticle-laden lymph nodes embedded in mesorectal fat, as would be the clinical scenario for diagnostic support of staging rectal cancer using magnetomotive ultrasound.

Results: The estimated reflection between the insert and bulk material was 10%, matching the clinical case of a lymph node within fat (9%). Speed of sound, attenuation, and Young's modulus of the bulk material were matched with those of body fat. The insert also matched the acoustic and elastic properties of lymph node tissue except for attenuation, which was lower than that given in the literature. Glass beads and graphite were used to control backscatter levels in the respective tissue mimics, providing a contrast of -3.8 dB that was consistent with clinical image appearance. The magnitude of magnetomotion remained stable in three separate samples over the course of 3 weeks.

Conclusion: We have developed a phantom for magnetomotive ultrasound that combines the stability of an oil-based bulk material with the necessity of using a water-based material for the insert. The production procedure may be applied to other phantoms where one tissue type needs to be embedded within another.

Introduction

Magnetomotive ultrasound (MMUS) is an emerging novel technique that enables superparamagnetic iron oxide nanoparticles to be used as a contrast agent for ultrasound [1]. A time-varying magnetic field acts to displace the nanoparticles, and as this motion is transferred to the surrounding tissue the resulting tissue vibration serves as a marker for the presence of nanoparticles.

This technique is presently employed within a medical device that is currently in the development phase. The goal of the device is to contribute to the health care system for rectal cancer diagnostics by providing more reliable detection of cancer spread to nearby lymph nodes, an important marker of cancer progression [2]. Like all medical devices under development, verification and validation are essential to ensure optimal functionality and fulfillment with regulatory requirements. Animal and/or human studies are often necessary for evaluation of clinical inquiries, while more technical parameters are more efficiently tested using phantoms, which is often preferred for ethical, economical, and

environmental reasons. As MMUS relies on ultrasound imaging, ultrasound tissue-mimicking phantoms [3,4] are the natural starting point for creating test objects. What sets an MMUS phantom apart is the inclusion of a magnetically labeled region, preferably using the same type of nanoparticles intended for clinical application.

Several additional requirements must be considered for a MMUS phantom, beyond accurately mimicking the acoustic properties of soft tissue. First, to ensure consistent behavior for repeatable measurements, the phantom material must be durable enough to withstand the aging processes, particularly those that could alter the properties of the nanoparticle compound. Moreover, acoustic parameters common to other ultrasound phantoms, such as sound speed, attenuation, and backscatter, must also remain stable.

Second, as contrast in a magnetomotive image is derived from nanoparticle motion, and this parameter is highly dependent on the viscoelastic properties, the capability to tune these is essential.

Third, for the specific case of rectal lymph nodes, these nodes are typically localized within the mesorectal fat, and in an ultrasound

* Corresponding author. Biomedical Engineering, Lasarettsgatan 37, 221 85, Lund, Sweden.

E-mail address: tomas.jansson@med.lu.se (T. Jansson).

image, they may appear darker than the surrounding fat tissue [5]. Thus, backscatter is another critical parameter to adjust to achieve this appearance.

Numerous materials have been suggested for the production of ultrasound tissue-mimicking phantoms, some of which are also used in MMUS research [6–10]; for example, imaging [8] and elastography [10]. None of the MMUS phantoms presented have, however, been optimized for a specific anatomical situation.

In general, tissue-mimicking materials can be categorized into water-based or oil-based types, with water-based typically being less durable than oil-based. Styrene-butylene/ethylene-styrene (SEBS) in mineral oil mixed with ballistic gel offers the advantage of tunable elasticity without significantly affecting sound speed [11]. However, nanoparticles for clinical use are dissolved in water and therefore do not mix with an oil-based matrix. This limitation necessitates the use of water-based materials such as gelatin [10] or polyvinyl alcohol (PVA) [8]. Notably, by varying the concentration of gelatin, the elasticity may be adjusted [10]. For PVA, a water solution can be made to polymerize by the solution undergoing sequences of freeze-thaw cycles [12], and its concentration in water as well as the number of freeze-thaw cycles determines the elasticity.

A drawback of water-based materials is that water tends to evaporate from the phantom, necessitating that it is completely sealed. Additionally, there is a risk of bacterial invasion, which may limit durability.

To meet the conflicting requirements of durability and water solubility, we propose the use of a bulk material consisting of an oil-based polymer (SEBS) with a sealed insert made from PVA containing the nanoparticles. This design mimics the anatomical scenario where magnetic nanoparticles accumulate in lymph nodes draining a tumor area after a peritumoral subcutaneous injection, following the proposed clinical strategy for MMUS.

To minimize reflection between the bulk material and the insert, here we suggested pouring the PVA solution into a designated cavity in the bulk material, followed by a freeze-thaw cycle of the entire volume. Sound speed and other acoustic parameters were adjusted to replicate the case of a rectal lymph node embedded in fatty tissue. Backscatter and attenuation were controlled by incorporating glass beads and graphite; graphite primarily regulates the desired attenuation, while glass beads adjust the backscatter. The stiffness of the bulk material was mainly determined by the concentration of SEBS to oil, whereas the stiffness of the insert depends on PVA concentration, along with the number of freeze-thaw cycles. Finally, the durability of the SEBS/PVA combination was tested over a 3 week period.

Methods

The aim of the phantom is to mimic a portion of the human rectum. However, as with all tissue phantoms, compromises were necessary to model this complex anatomical structure. Anatomically, the lymph nodes of interest are located a few millimeters to a maximum of 3 cm away from the rectal wall [13] and are embedded in the mesorectal fat that surrounds the rectum. As the thickness of the rectal wall is only a few millimeters (2.14 ± 0.54 mm [14]) and not the focus of this application, only the mesorectal fat with an embedded lymph node was modeled. This simplification may pose a limitation, as the rectal wall could introduce a phase-aberrating effect. However, as the rectal wall is stationary, it is less likely to affect magnetomotion estimation, similar to how the morphology of overlying tissues has a limited impact on blood flow velocity measurements. Depending on the extent of phase aberration, it could potentially degrade the focus, resulting in a blurrier image. Nevertheless, because the primary purpose of the phantom is to evaluate magnetomotion rather than image quality, phase-aberrating effects from the rectal wall were not considered in the phantom design.

Due to its complexity and small size, the internal structure of the lymph node itself was not modeled and an even distribution of nanoparticles within the node was assumed, as would be expected for healthy

lymph nodes (metastases are visualized as particle-free voids within the node [15,16]). The two different parts of the phantom are henceforth referred to as the bulk material and the insert, mimicking the mesorectal fat and the lymph node, respectively. These should resemble the real tissue from an acoustic and mechanical point of view, and thus speed of sound, backscatter, attenuation coefficient, and elasticity were considered in the model.

Phantom construction

The manufacturing process for the bulk material and the insert, as well as their integration into a single unit, is outlined below. Each material has a section detailing general design requirements, followed by a section on the fabrication of each component.

Bulk—general design requirements

The bulk part of the phantom was made of SEBS-type copolymers mixed in mineral oil with added ultrasound scatterers. This specific copolymer was chosen for its tunable viscoelasticity and acoustic properties, which closely resemble those of human tissue. Notably, it offers temporal stability in its Young's modulus as well as speed of sound and attenuation measurements similar to that of human fat [17]. Additionally, SEBS phantoms are homogeneous, easy to produce, non-toxic, and relatively inexpensive. Composition of the phantom was initially based on the formulation proposed by Oudry et al. [17], but the parameters were modified to more accurately match the conditions modeled in this study.

The aim was to have a Young's modulus resembling human fat, measured by Samani et al. [18] to be 3 ± 1 kPa. In polymerized SEBS, the Young's modulus increases with concentration following the relation (Eqn [1]) given by Oudry et al.:

$$E = 0.16c^{2.46} \quad (1)$$

where E is the Young's modulus in kPa and c is the SEBS concentration in weight percentage (wt%). This relation shows that the 4 wt% concentration suggested by Oudry et al. was too high (4.84 kPa) and was therefore decreased to 3 wt% to fall within the range for human fat given above (2.38 kPa).

Attenuation is commonly adjusted in phantoms by adding graphite, but in SEBS it was found to cause excessive attenuation at the targeted frequency of 10 MHz. The attenuation coefficient for human breast fat was found by d'Astous and Foster [19] to obey the relation 0.158 ± 0.03 dB/(cm MHz^{1.7}), valid between 3 and 7 MHz. However, a wide range of values with large uncertainty has been reported for human fat, even up to several dB cm⁻¹ MHz⁻¹ [20,21]. Based on observations from our ongoing clinical study, we chose to evaluate the relation by d'Astous and Foster at 10 MHz. This calculation resulted in a value of 7.9 dB/cm, a value more closely achieved by adding glass beads only at a concentration of 3 wt%.

The speed of sound in mesenteric fat was found by Errabolu et al. [22] to be 1427 m s⁻¹, while for fat tissues in general it can reach up to 1470 m s⁻¹ [20,23].

Bulk material preparation

The bulk material was prepared in an autoclave bottle. In total, 94 g of mineral oil with a dynamic viscosity of 14.2–17 mm² s⁻¹ at 40°C (catalog no. 330779, Sigma-Aldrich, Darmstadt, Germany) and 3 g of SEBS (Kraton G 1650E, Kraton Polymers, Houston TX, USA) were mixed before being heated in a temperature-controlled oven (VWR DRY-Line, VWR, Radnor PA, USA) at 120°C for 2 h. A stirrer magnet was placed inside the bottle prior to heating to prevent the formation of gas bubbles when placed on the hot plate. At this step, only 90% of the final mineral oil mass was used. The remaining 10% was reserved to pre-mix the glass bead powder (type A2429 glass, Potters Industries, Malvern, PA, USA) before adding it to the main solution. This approach helped to prevent

glass bead aggregates, maintaining a concentration 3 wt% of the total solution. Once this secondary solution was homogeneously mixed, it was added to the heated SEBS solution and stirred at 500 rpm for 5 min. This speed was chosen as a balance between preventing bead sedimentation and ensuring an even distribution of heat throughout the solution.

After mixing, the mixture was slowly and carefully poured into the mold (Fig. 1) and allowed to cool at room temperature, during which the gel formed. The temperature of the solution during pouring was critical; if too low, it may trap bubbles that form while pouring the viscous liquid. Conversely, if poured when too hot, the glass beads may have time to sediment before the solution solidifies. A total of 20 mL of the bulk solution was reserved and kept at room temperature to be used as a sealant at a later stage. Note that from this point, the gel could be reused by re-heating it.

Solutions with glass bead concentrations of 0, 1, and 2 wt% were prepared similarly.

Insert—general design requirements

The nanoparticles used were water-soluble, necessitating a water-based phantom material. For this reason, a PVA polymer was chosen as the material for the insert. As the insert was designed to be encapsulated in the bulk material, we hypothesized that water evaporation from the PVA should not be an issue for the phantom's durability. The production method of the insert was inspired by Surry et al. [12]. However, the parameters were adjusted to achieve an acceptable balance between viscoelastic and acoustic properties to better resemble a human lymph node.

For modeling magnetotomotion, the principal parameter for the insert was Young's modulus, which should reflect the elastic properties of a lymph node. For axillary lymph nodes, this was measured at 6.9 ± 0.5 kPa [24]. In a PVA phantom, elasticity depends on PVA concentration as well as the number of freeze-thaw cycles applied during fabrication. Several studies have suggested different PVA concentrations and freeze-thaw cycles to simulate biological tissue [25–29]. Three PVA concentrations of 10, 12.5, and 15 wt% at a single freeze-thaw cycle were evaluated under these conditions based on Young's modulus reported by Gordon [26] to find the best match for the aforementioned lymph nodes.

Sound attenuation in human lymph nodes has been measured as $0.58 \text{ dB cm}^{-1} \text{ MHz}^{-1}$ [30]; however, unclear over what frequency range. As lymph nodes appear darker than their surrounding in an ultrasound image, graphite was preferred to achieve this appearance because it produces less scattering than glass beads. Additionally, graphite is able to increase attenuation to levels similar to those of lymph nodes. Note, however, that it was not possible to reach the desired attenuation by adding more graphite, as this would have increased echogenicity too

much. Concentrations of 5, 15, and 30 mg mL^{-1} were investigated for sound speed, attenuation, and Young's modulus, as well as apparent backscatter relative to the bulk tissue.

Sound speed in human lymph nodes was found by the same investigators to be 1514 m s^{-1} [30].

Insert preparation

The material for the three inserts was made from PVA powder (Molecular weight 89,000–98,000, 99 + % hydrolyzed, product no. 341584, Sigma-Aldrich, Darmstadt, Germany) at mass fractions of 10, 12.5, and 15 wt%. These were mixed with water to a total weight of 100 g for each sample and then heated in the oven at 100°C for 1 h. Water evaporation was compensated by adding water to maintain the correct PVA concentration. After heating, graphite powder was added at 5, 15, and 30 mg mL^{-1} for the 15 wt% PVA solution and mixed with a magnetic stirrer for 5 min at 500 rpm. The nanoparticles (Ferumoxtran-10, Ferrotan SPL Medical B.V., Nijmegen, The Netherlands) were prepared at different concentrations of 0.5, 1, 2, and 4 mg mL^{-1} and then directly added to the PVA and graphite solution. The preparation was left at room temperature to allow air bubbles to rise to the surface, which occurred spontaneously due to the solution's low viscosity.

Solidification and polymerization of the PVA was induced by one freeze-thaw cycle of the entire bulk-insert combination (see the Measurements section below for phantom properties/Young's modulus).

Bulk and insert combination—general design requirements

Due to the different properties of the base materials, it was found that the best way to avoid trapping air between them was to pour the insert in its molten form directly into a suitable cavity within the bulk material. Even so, the difference in acoustic impedance between the two substances should be similar to that observed *in vivo*. Fat, lymph nodes, and water have an acoustic impedance of 1.33×10^6 , 1.6×10^6 , and $1.48 \times 10^6 \text{ kg m}^{-2} \text{ s}^{-1}$, respectively [31], while mineral oil has an acoustic impedance of $1.21 \times 10^6 \text{ kg m}^{-2} \text{ s}^{-1}$ [32]. Calculating the reflection coefficient for the two cases (with the PVA solution assigned the acoustic impedance of water) showed that the estimated reflection in the phantom was 10% compared with 9% in the tissue case. This calculation also neglects the influence of scattering from the presence of graphite and glass beads, or cellular structures in tissue.

The geometry of the final phantom was designed to allow imaging of the nanoparticle-laden insert from four directions by placing the transducer in semi-circular cutouts on each side of the insert (Fig. 1). The insert was positioned to reflect the range of depths at which lymph nodes are typically found in humans [13]. The height of the phantom was set at 10 mm, significantly greater than the elevation of the ultrasound image slice, providing some margin for placement of the transducer, including tilt.

Bulk and insert preparation

The mold for the bulk material was designed with a solid rod-shaped negative mass measuring 5 mm in diameter and 10 mm in height. After the gel had solidified and the rod was removed, the PVA solution could be poured into the hole left by the rod.

Before undergoing the freeze-thaw cycle, the insert solution was poured into the hole left in the bulk with the help of a syringe, which was tilted to minimize air bubbles. The bulk and insert ensemble were then placed in the freezer, with a single freeze-thaw cycle consisting of 18 h in the freezer at $-20 \pm 2^\circ\text{C}$ followed by 2 h at room temperature.

After the freeze-thaw cycle, the remaining SEBS solution was reheated in the oven at $100 \pm 5^\circ\text{C}$ for 30 min and then poured over the hole containing the PVA insert, ensuring it was entirely enclosed by SEBS and thereby preventing exposure to air.

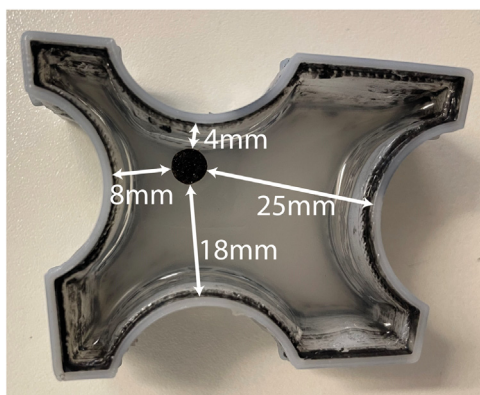


Figure 1. Top view of the phantom showing the different distances (white arrows) between the insert (black) and the semi-circular cutouts on the sides where the probe can be placed. The distances exclude the phantom wall, which is 2.5 mm. The insert has a diameter of 5 mm.

Measurement of phantom properties

Young's modulus

The Young's modulus of both material components of the phantom, the bulk material and the insert, was measured individually using separately molded $75 \times 35 \times 35$ mm blocks prepared as described for each material (the PVA also underwent one 18 h freeze-thaw cycle). The material samples were positioned on a weight scale and compressed using a translation stage. This setup allowed measurement of both the applied force and the change in length, which were then used to calculate stress and strain.

For the bulk material, stress and strain were plotted and the Young's modulus was obtained from linear regression between the two variables. The PVA samples exhibited a more non-linear behavior between stress and strain, so the mean static Young's modulus value was determined as the slope of this relationship in a strain range between 3% and 8%, as done by Duboeuf et al. [29].

Speed of sound

The sound speed in the SEBS bulk material samples was measured using a 2 MHz transducer driven by a pulser receiver (Panametrics 5052PR, Olympus NDT Inc, Waltham, MA, USA) set in pulse-echo mode. The phantom was placed in a water tank, and echoes from the front and back walls were recorded on an oscilloscope. Sound speed was determined by measuring both the length of the phantom sample (multiplied by two) and the time elapsed between the echoes.

The high attenuation made pulse-echo measurement challenging for the PVA insert samples, so the through-transmission technique described by Chen et al. [33] was used instead. During the measurements the temperature was 19°C , which was used to calculate the sound speed in water according to Lubbers and Graaff [34].

Measuring the length of the PVA samples proved difficult due to the softness of the material and the uneven surface left open to transmit sound. As a result, the length measurement had relatively low accuracy (75 ± 0.5 mm), leading to higher uncertainty in sound speed measurements.

Attenuation coefficient

The attenuation coefficient of each part of the phantom was measured by transmitting ultrasound pulses through the rectangular samples (75×35 mm) along their long and short axes, respectively. A 10 MHz transducer (Olympus A327S-SU, Olympus NDT Inc.) was placed coaxially in front of a 0.5 mm hydrophone (Precision Acoustics, Higher Bockhampton, Dorchester, UK) in a water tank, with the sample positioned between them. The transducer was driven by a pulser/receiver (Panametrics 5052PR, Olympus NDT Inc.). After fast Fourier transform calculations of the received signals, the power spectra (expressed in dB) from the two cases were subtracted, yielding the power lost over the length corresponding to the difference between the length and the width (40 mm) for each sample, for each frequency component within the usable bandwidth for the received signals. The attenuation emanating from the added water path when measuring the short axis was much less than the expected measurement errors and was not accounted for. This method minimized errors caused by reflections occurring at the sample interfaces.

Magnetomotive displacement measurements

A MMUS imaging system from NanoEcho AB (Lund, Sweden) was used to measure material displacement induced by the magnetic field generated by the system. This system is described by Jansson et al. [2], but in a version that is now updated with a center frequency of the transducer elements of 10 MHz. Displacement in the samples for each nanoparticle concentration (0.5, 1, 2, and 4 mg mL⁻¹ at a PVA concentration of 14%) was calculated as the average displacement recorded within a circular region of interest, drawn slightly smaller than the insert in the ultrasound image (diameter of 4.5 mm). The final displacement value was determined as the average of three individual measurements taken

at different image planes. The limited thickness of the phantom allowed for only three independent planes—at the center, near the top, and near the bottom—facilitating repeatable measurements.

Assessment of durability

Three additional phantoms were produced according to the procedure outlined above and stored at room temperature. Over a period of 3 weeks, the weight and magnetomotive displacement of each phantom were recorded nearly every other day. The regions of interest were selected as previously described, and the distance in the ultrasound image from the transducer face to the center of the insert was noted for each measurement.

Results

Bulk

Young's modulus

The Young's modulus for the bulk was found to be 2.1 ± 0.5 kPa for a copolymer concentration of 3 wt%, as shown by the graph equation in Figure 2 ($R^2 = 0.99$). The theoretical values computed according to eqn (1) predict a Young's modulus of 2.38 kPa.

Acoustic properties

The speed of sound was measured to be 1401 m s^{-1} , with a standard deviation of 10 m s^{-1} ($n = 3$). The attenuation co-efficient increased with glass bead concentration and ranged between 3.6 and 7.1 dB cm^{-1} at 10 MHz for glass bead concentrations of 0, 1, 2, and 3 wt% (Fig. 3).

Insert

Young's modulus

Young's modulus was evaluated for the three different PVA concentrations of 10, 12.5, and 15 wt%, all with one freeze-thaw cycle (Fig. 4). Young's modulus values were found to be 3.9 ± 1.3 , 6.0 ± 1.2 , and 7.8 ± 2.5 kPa, respectively. The concentration of graphite in the insert was kept at 15 mg mL^{-1} for all PVA concentrations.

Acoustic properties

The speed of sound was measured for different PVA and graphite concentrations. No trend could be identified, so the speed of sound in PVA was determined as an average of 1521 m s^{-1} with a standard deviation of 21 m s^{-1} for all PVA concentrations (10, 12.5, and 15 wt%, with three samples at each concentration) and all graphite

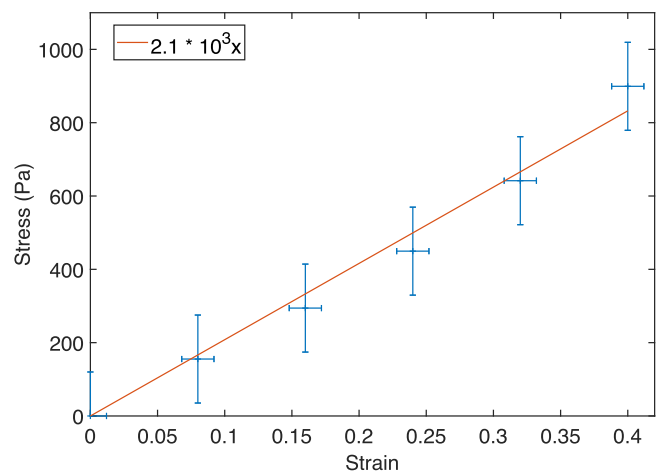


Figure 2. Stress-strain relation for the styrene-butylene/ethylene-styrene gel modeling the bulk (the indicated uncertainty reflects the uncertainty due to length measurements). The linear regression equation is shown, $R^2 = 0.99$.

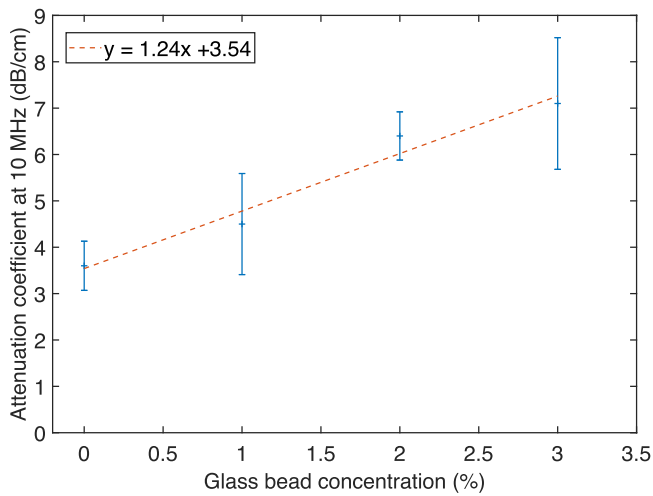


Figure 3. Sound attenuation coefficient for styrene-butylene/ethylene-styrene gel (3 wt%) containing different concentrations of glass beads in dB cm^{-1} at 10 MHz. The graph also shows the linear regression and its equation, as well as the standard deviation as error bars ($n_{\text{total}} = 12$). $R^2 = 0.99$.

concentrations (5, 15, and 30 mg mL^{-1} at 15 wt% PVA), giving a total of 18 measurements.

The attenuation coefficient was found to increase with the concentration of graphite in the PVA phantom, as seen in Figure 5. At 15 mg mL^{-1} the attenuation was found to be $0.19 \text{ dB cm}^{-1} \text{ MHz}^{-1}$, less than the reported value of $0.58 \text{ dB cm}^{-1} \text{ MHz}^{-1}$ for lymph nodes [30].

Bulk and insert

Displacement

The magnetomotive displacement in the phantom, induced by nanoparticle motion, was measured under different conditions. First, Figure 6 confirms the expected linear relationship between displacement and the nanoparticle concentration. Second, Figure 7 illustrates how displacement decreases with an increasing distance between the magnet and the insert at different nanoparticle concentrations. Additionally, the results show that higher particle concentrations result in higher displacement.

Acoustic properties

The insert modeling the lymph node appeared darker than the bulk material modeling the fat in images taken with the NanoEcho system

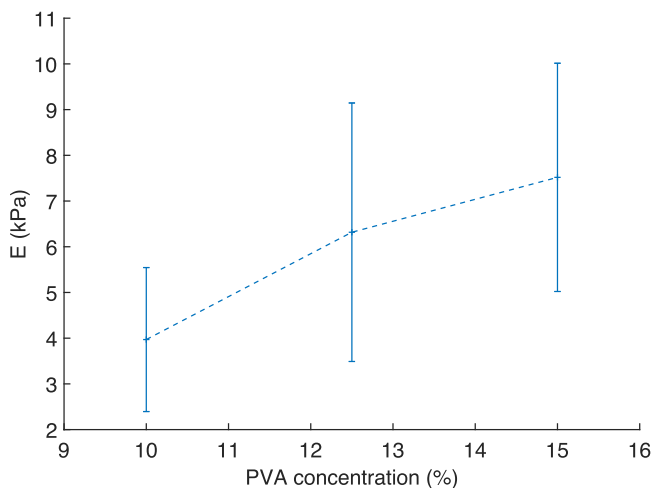


Figure 4. Young's modulus for varying polyvinyl alcohol concentrations, one freeze-thaw cycle ($n = 4$ at each concentration).

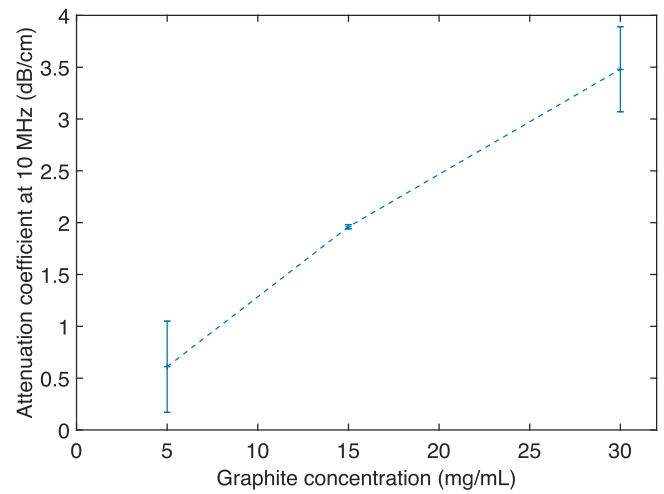


Figure 5. Attenuation co-efficient at 10 MHz in polyvinyl alcohol for different graphite concentrations. The error bars show the standard deviation for individual measurements at 10 MHz ($n_{\text{total}} = 6$).

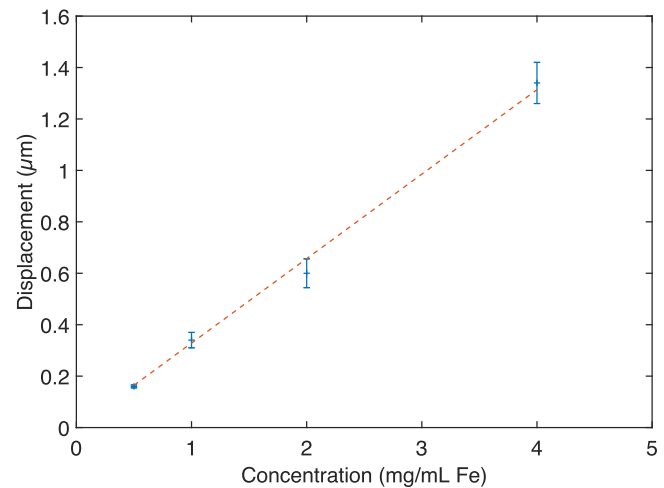


Figure 6. Magnetomotive displacement as a function of the nanoparticle concentration at approximately 12 mm distance from the transducer face ($n = 3$ per concentration).

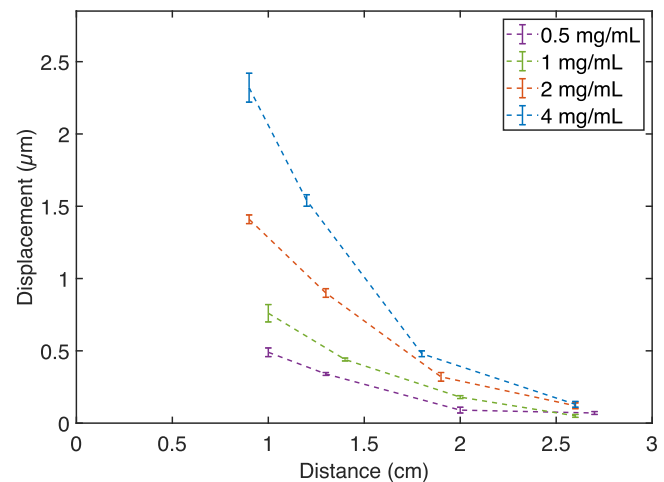


Figure 7. Displacement as a function of the distance between the insert and the probe at different concentrations of nanoparticles. Distances vary somewhat for different samples due to the amount of gel applied.

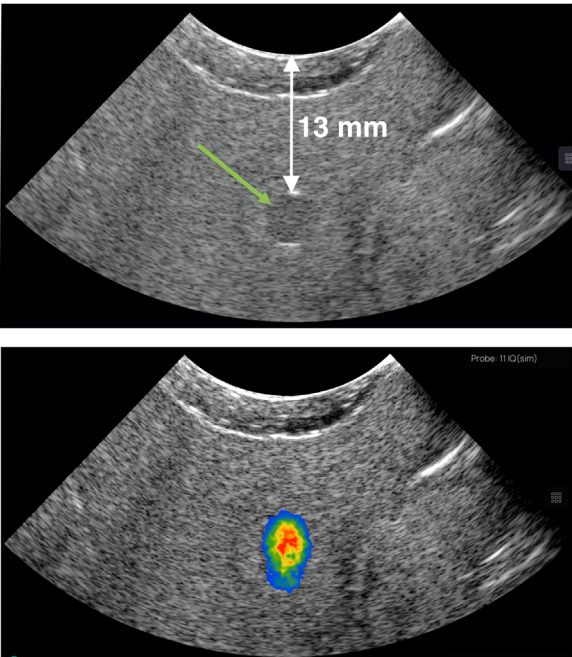


Figure 8. (Top panel) The insert in the phantom appears darker in the ultrasound B-mode image (green arrow). The distance to the transducer is 13 mm (white arrow), including the wall and a layer of ultrasound gel. (Lower panel) The same image but with a color overlay representing magnetomotive displacement (red is the highest, corresponding to $1.37 \mu\text{m}$) as presented to a user. The nanoparticle concentration is 2 mg mL^{-1} in this case, and the average displacement within a region of interest drawn in the B-mode image to encircle the insert is $1.08 \mu\text{m}$.

(Fig. 8, top panel). The contrast difference (calculated from radio frequency ultrasound data) between the bulk material and the insert was $-3.8 \pm 0.5 \text{ dB}$, which is less than that observed for lymph nodes in the ongoing study referenced by Jansson et al. [2], where the contrast difference for observable lymph nodes was in the range of -7 to -10 dB . However, this contrast level is within the range observed in earlier clinical studies [5].

The lower panel in Figure 8 shows the same B-mode image but with the corresponding estimated magnetomotive signal overlaid as a color code. Red corresponds to the highest detected magnetomotion, which in this case was $1.37 \mu\text{m}$, and blue indicates the lowest detected motion.

The average detected motion within the region of interest that encircled the insert, as drawn in the B-mode image, was $1.08 \mu\text{m}$. The nanoparticle concentration for this measurement was 2 mg mL^{-1} .

Experimentally measured parameters for the bulk material and the insert are presented in Table 1. The upper part of the table summarizes the values found in tissues, as discussed in the Methods section; the middle section shows values found in the literature for both types of materials; and the bottom part shows values measured during the experiments.

Assessment of durability

In Figure 9a–c the recorded magnetomotive displacements during the course of 3 wk for the three phantoms can be seen as blue crosses connected with a blue solid line (scale on the left). The error bars indicate the standard deviations for each estimated average displacement within the region of interest. In each panel the distance is also plotted in the ultrasound image from the transducer face to the center of the region of interest (red crosses and dashed lines, scale to the right). Visual inspection of the graphs reveal that there is no clear trend for any change of the magnitude of magnetomotion. Linear regression confirmed this with p values of 0.33, 0.06, and 0.24, respectively, for cases A through C ($p < 0.05$ was considered significant).

The phantoms lost between 0.14% and 0.15% of their weight per day, resulting in a total weight loss of 2.3%–2.4% over the 3 wk. This weight loss was statistically significant ($p < 0.001$), but apparently this reduction in weight did not affect the magnitude of magnetomotion.

Discussion

Here we have demonstrated the preparation process of a tissue-mimicking phantom for MMUS, with relevant mechanical and acoustical parameters for the case of a lymph node embedded in mesorectal fat. The sound speeds were matched for the two tissue types, as well as the attenuation. Backscatter was adjusted to create a -3.8 dB difference in echogenicity between the insert and the bulk material, such that the bulk material had higher backscatter relative to the insert, consistent with the images acquired in our ongoing study. We typically observed a larger contrast difference, but the status of the observed lymph nodes was unknown. In the literature, lymph nodes in patients may appear in a range from dark to having no contrast difference at all, where a dark lymph node is an (uncertain) marker of malignancy [5]. As the primary purpose of the phantom is to evaluate magnetomotion rather than to train clinicians to detect lymph nodes, contrast was a lower priority but it can be adjusted according to need.

Table 1
Relevant properties of biological tissues and the phantom components

Medium type	Sound speed (m/s)	Young's modulus (kPa)	Attenuation coefficient (dB/cm/MHz)	Acoustic impedance (MPa s/m)	Contrast at 11 MHz (dB) ^a
Tissue					
Fat	1427 [22] (mesorectal)	3 ± 1 [18]	$0.158 \pm 0.03 \text{ dB/(cm MHz}^{1.7})$ [19]	1.33 [31]	–
Lymph node	1514 [30]	6.9 ± 0.5 [24]	0.58 [30]	1.6 [35]	–(0–10) [unpublished data,5]
Phantom – literature					
SEBS bulk	1424 [17]	2.38 ± 0.5 [17]		1.21 [32] ^b	NA
PVA insert	1520–1540 [12]	$4.5\text{--}8.6$ [26] ^c		1.48 ^b	NA
Phantom – experiments					
SEBS bulk	1401 ± 10	2.1 ± 0.5	$0.36\text{--}0.71$ ^d		–
PVA insert	1521 ± 21	6.3 ± 2.8 ^e	0.19 ± 0.002		-3.8 ± 0.5

NA, not available; PVA, polyvinyl alcohol; SEBS, styrene-butylene/ethylene-styrene.

^a dB-values are given as contrast to the bulk material. For tissue, the values is an observed range from an ongoing study.

^b Acoustic impedance of water and oil, respectively.

^c Range of values for 10, 12.5, and 15 wt% PVA, one freeze-thaw cycle.

^d Range of values for 0%–4% glass bead concentration.

^e Value at 12.5 wt% PVA.

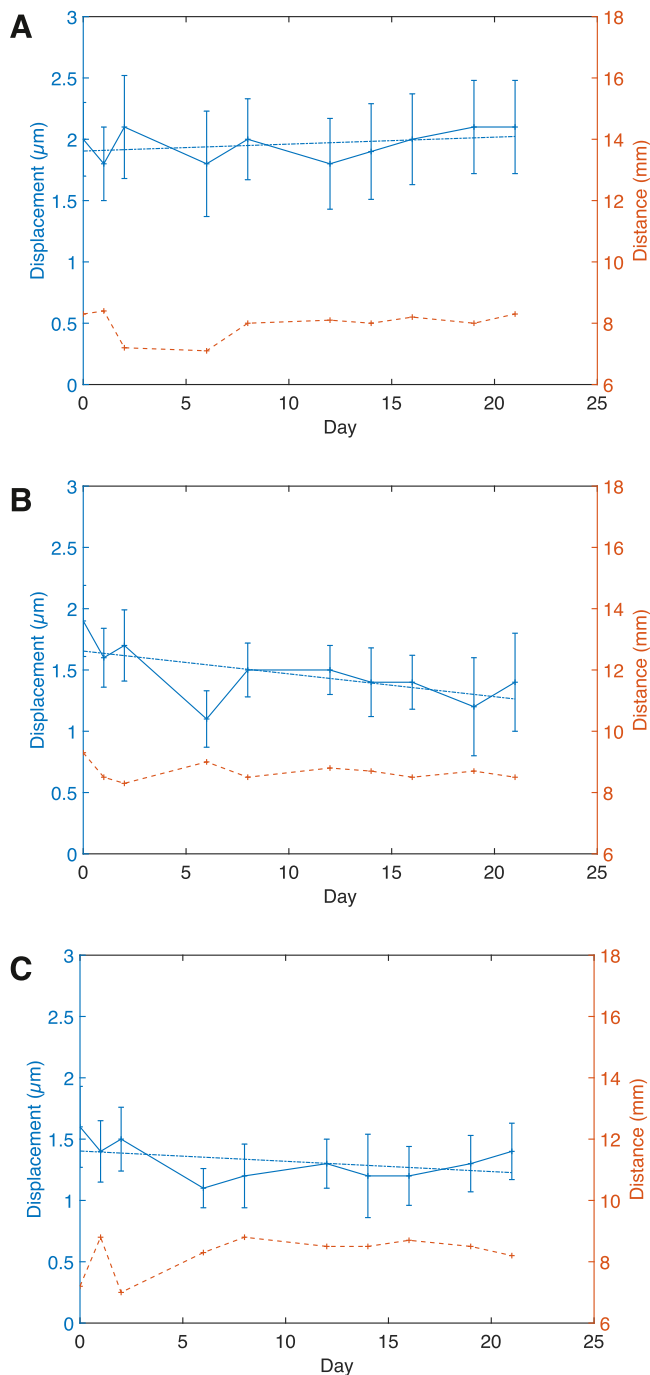


Figure 9. Recorded displacements (blue) and transducer to insert distances (red) for the three phantoms (a–c) over the measured time period of 3 wk. The error bars indicate the standard deviations for each estimated average displacement within the region of interest.

The graphite concentration needed to be carefully balanced relative to the glass bead concentration to achieve a realistic contrast difference while maintaining a suitable attenuation at the frequency of interest (10 MHz here). Although the resulting attenuation was less than what has been reported for lymph nodes, the effect is minimal from an imaging perspective due to the short acoustic path length through the insert, which was only a few millimeters. This reduced attenuation is of even less consequence for magnetomotion.

The most important imaging factor, however, is that the reflection between the insert and bulk material matches the clinical situation. Earlier phantom prototypes with higher reflection made it difficult to track magnetomotion inside the insert due to signal loss. Another potential

source of artifacts is refraction, which is determined by the ratio of sound speeds between the two media. As shown in Table 1, the ratio of sound speeds for the phantom materials now matches the clinical case (0.921 and 0.943, respectively), suggesting that any refraction effects should also be similar.

In the phantom, the lymph node inclusion contained a water solution of magnetic nanoparticles, making it incompatible with the SEBS/mineral oil mixture. A separate inclusion made from PVA was tested and inserted into the background material but achieving a close fit between the two materials was challenging, causing the border between them appear too bright in the ultrasound image. To address this issue, the PVA solution was poured into a preformed hole in the SEBS and the entire phantom was then subjected to a freeze-thaw cycle. This process eliminated unwanted reflections from trapped air.

Young's modulus is the most important factor for magnetomotive displacement, and the Young's moduli for the bulk and insert matched those of fat and axillary lymph nodes. The reported elasticity value for an axillary lymph node [24] falls between the measured elasticities for the 12.5 and 15 wt% PVA (within one standard deviation), so either could be used. However, due to a calculation error, the PVA concentration used for displacement measurements was 14 wt% instead of the intended 15 wt%. The effect was considered relatively minor compared with 15 wt%, and the displacement for the 12.5 wt% would be higher regardless, as it is less stiff.

The model is not complete in the sense that the rectal wall is not included. In a patient the tissue layers of the rectal wall act as a phase screen, which could lead to potential focus degradation. If the rectal wall remains stationary it will not affect the estimation of magnetomotion, which is based on phase shifts between subsequently received echoes from the nanoparticle-laden area. These phase shifts result from the motion of nanoparticles and will not be influenced by a stationary phase screen, although some image blurring could occur. As the primary aim of the phantom is to evaluate magnetomotion rather than image quality, modeling the rectal wall has been omitted.

The phantom was shown to provide consistent magnetomotive displacements over a 3 wk period, despite being left at room temperature during this time. Weight loss was attributed to the release of mineral oil from the phantoms, as their surfaces became oily over the test period.

The resulting phantom is expected to be useful for evaluating equipment for MMUS imaging, particularly in applications related to rectal cancer. The manufacture of test objects for other clinical scenarios is likely to start with the procedures described here. Additionally, the experiences gained from this study may be valuable for developing other phantoms where one tissue type needs to be embedded in another.

Conclusion

Here we have demonstrated the fabrication of a tissue phantom suitable for magnetomotive imaging. The phantom mimicked the scenario of a magnetic nanoparticle-laden lymph node embedded in fat. Of particular importance was the matching of Young's moduli for the two tissue types, as the magnetomotive signal depended on the motion induced by nanoparticles exposed to a time-varying magnetic field. Due to the production method, reflections between the bulk material and the insert were avoided. The resulting B-mode image resembled the clinical case with healthy lymph nodes, even though echogenicity and attenuation may vary significantly *in vivo* depending on lymph node status. However, these parameters had a minor impact on magnetomotive displacement.

Data availability

The data that support the findings of this study are available from the corresponding author (T.J.), upon reasonable request.

Declaration of generative AI and AI-assisted technologies in the writing process

During the preparation of this work the authors used the writing assistant functionality of ChatGPT in order to improve the language of the manuscript. After using this service, the authors reviewed and edited the content as needed and take full responsibility for the content of the publication.

Conflict of interest

A.M., M.S., and L.P. are full-time employees at NanoEcho AB, and each own shares in the company (<1%); T.J. owns shares in NanoEcho AB (<1%). J.R. declares no conflict of interest.

Acknowledgments

The authors gratefully acknowledge Prof. Carmel Moran for helpful comments on the manuscript. The study was supported by The Skåne Regional Council and by a grant from the Fru Berta Kamprad Foundation (FBKS-2023-27).

References

- [1] Sjöstrand S, Evertsson M, Jansson T. Magnetomotive ultrasound imaging systems: Basic principles and first applications. *Ultrasound Med Biol* 2020;46(10):2636–50.
- [2] Jansson T, Jansson L, Mousavi A, Persson L, Angenete E. Detection of magnetomotive ultrasound signals from human tissue. *Nanomedicine* 2023;47:102621.
- [3] Zell K, Sperl JI, Vogel MW, Niessner R, Haisch C. Acoustical properties of selected tissue phantom materials for ultrasound imaging. *Phys Med Biol* 2007;52:N475.
- [4] McGarry CK, Grattan LJ, Ivory AM, Leek F, Liney GP, Liu Y, et al. Tissue mimicking materials for imaging and therapy phantoms: A review. *Phys Med Biol* 2020;65(23).
- [5] Edelman BR, Weiser MR, ultrasound Endorectal. Its role in the diagnosis and treatment of rectal cancer. *Clin Colon Rectal Surg* 2008;21:167–77.
- [6] Madsen EL, Zagzebski JA, Banjavic RA, Jutila RE. Tissue-mimicking materials for ultrasound phantoms. *Med. Phys.* 1978;5:391–4.
- [7] Burlew MM, Madsen EL, Zagzebski JA, Banjavic RA, Sum SW. A new ultrasound tissue-equivalent material. *Radiology* 1980;134(2):517–20.
- [8] Evertsson M, Cinthio M, Fredriksson S, Olsson F, Persson HW, Jansson T. Frequency and phase sensitive magnetomotive ultrasound imaging of superparamagnetic iron oxide nanoparticles. *IEEE Trans Ultrason Ferroelec and Freq Contr* 2013;60:481–91.
- [9] Cabrelli LC, Grillo FW, Sampaio DRT, Carneiro AAO, Pavan TZ. Acoustic and elastic properties of glycerol in oil-based gel phantoms. *Ultrasound Med Biol* 2017;43:2086–94.
- [10] Levy BE, Oldenburg AL. Elastometry of clot phantoms via magnetomotive ultrasound-based resonant acoustic spectroscopy. *Phys Med Biol* 2022;67(15). doi: 10.1088/1361-6560/ac7ea5.
- [11] Sjöstrand S, Meirza B, Grassi L, Svensson I, Camargo LC, Pavan TZ, et al. Tuning viscoelasticity with minor changes in speed of sound in an ultrasound phantom material. *Ultrasound Med Biol* 2020;46(8):2070–8.
- [12] Surry KJM, Austin HJB, Fenster A, Peters T. Poly(vinyl alcohol) cryogel phantoms for use in ultrasound and MR imaging. *Phys Med Biol* 2004;49(24):5529–46.
- [13] Topor B, Acland R, Kolodko V, Galanduk S. Mesorectal lymph nodes: Their location and distribution within the mesorectum. *Dis Colon Rectum* 2003;46(6):779–85.
- [14] Haber HP, Benda N, Fitzke G, Lang A, Langenberg M, Riethmüller J, et al. Colonic wall thickness measured by ultrasound: Striking differences in patients with cystic fibrosis versus healthy controls. *Gut* 1997;40(3):406–11.
- [15] Koh DM, George C, Temple L, Collins DJ, Toomey P, Raja A, et al. Diagnostic accuracy of nodal enhancement pattern of rectal cancer at MRI enhanced with ultrasmall superparamagnetic iron oxide: Findings in pathologically matched mesorectal lymph nodes. *Am J Roentgenol* 2010;194:W505–13.
- [16] Fortuin AS, Bruggemann R, van der Linden J, Panfilov I, Israël B, Scheenen TWJ, et al. Ultra-small superparamagnetic iron oxides for metastatic lymph node detection: Back on the block. *Wiley Interdiscip Rev Nanomed Nanobiotechnol* 2018;10(1):e1471.
- [17] Oudry J, Bastard C, Miette V, Willinger R, Sandrin L. Copolymer-in-oil phantom materials for elastography. *Ultrasound Med Biol* 2009;35(7):1185–97.
- [18] Samani A, Zubovits J, Plewes D. Elastic moduli of normal and pathological human breast tissues: An inversion-technique-based investigation of 169 samples. *Phys Med Biol* 2007;52(6):1565–76.
- [19] D'Astous FT, Foster FS. Frequency dependence of ultrasound attenuation and backscatter in breast tissue. *Ultrasound Med Biol* 1986;12:795–808.
- [20] Goss SA, Johnston RL, Dunn F. Comprehensive compilation of empirical ultrasonic properties of mammalian tissues. *J Acoust Soc Am* 1978;64:423–57.
- [21] Bamber JC. Ultrasonic attenuation in fresh human tissues. *Ultrasonics* 1981;19(4):187–8.
- [22] Errabolu RL, Sehgal CM, Bahn RC, Greenleaf JF. Measurement of ultrasonic nonlinear parameter in excised fat tissues. *Ultrasound Med Biol* 1988;14:137–46.
- [23] Duck FA. Physical properties of tissue—a comprehensive reference book. London: Academic Press; 1990.
- [24] Jung JW, Je H, Lee SK, Jang Y, Choi J. Two-dimensional shear wave elastography of normal soft tissue organs in adult beagle dogs; Interobserver agreement and sources of variability. *Front Bioeng Biotechnol* 2020;8:979. doi: 10.3389/fbioe.2020.00979.
- [25] Fromageau J, Gennissou JL, Schmitt C, Maurice RL, Mongrain R, Cloutier G. Estimation of polyvinyl alcohol cryogel mechanical properties with four ultrasound elastography methods and comparison with gold standard testings. *IEEE Trans Ultrason Ferroelectr Freq Control* 2007;54(3):498–509.
- [26] Gordon M. Controlling the mechanical properties of PVA hydrogels for biomedical applications. Dissertation. Canada: The University of Western Ontario; 1999.
- [27] Wang BH, Campbell G. Formulations of polyvinyl alcohol cryogel that mimic the biomechanical properties of soft tissues in the natural lumbar intervertebral disc. *Spine* 2009;34:2745–53.
- [28] Gautam UC, Pydi YS, Selladurai S, Das CJ, Thittai AK, Roy S, et al. A poly-vinyl alcohol (PVA)-based phantom and training tool for use in simulated transrectal ultrasound (TRUS) guided prostate needle biopsy procedures. *Med Eng Phys* 2021;96:46–52.
- [29] Duboeuf F, Basarab A, Liebgott H, Brusseau E, Delachartre P, Vray D. Investigation of PVA cryogel Young's modulus stability with time, controlled by a simple reliable technique. *Med Phys* 2009;36(2):656–61.
- [30] Yongchen S, Yanwu D, Jie T, Zhensheng T. Ultrasonic propagation parameters in human tissues. *Ultrasonics Symp Proc* 1986:905–8.
- [31] Hoskins P, Martin K, Thrush A, editors. Diagnostic Ultrasound: Physics and Equipment. 2nd ed. Cambridge: Cambridge University Press; 2010.
- [32] Lifshitz I, Pedersen P, Lewin P. Reconstruction of the acoustical impedance profile of a multilayer medium. *Ultrason Imaging* 1992;14(1):40–68.
- [33] Chen P, Pollet AMAO, Panfilova A, Zhou M, Turco S, den Toonder JMJ, et al. Acoustic characterization of tissue-mimicking materials for ultrasound perfusion imaging research. *Ultrasound Med Biol* 2022;48(1):124–42. doi: 10.1016/j.ultrasmed-bio.2021.09.004.
- [34] Lubbers J, Graaff R. A simple and accurate formula for the sound velocity in water. *Ultrasound Med Biol* 1998;24(7):1065–8.
- [35] Hildebrandt U, Klein T, Feifel G, Schwarz HP, Koch B, Schmitt RM. Endosonography of pararectal lymph nodes. *In vitro* and *in vivo* evaluation. *Dis Colon Rectum* 1990;33(10):863–8.